

Toward augmenting tip-enhanced nanoscopy with optically resolved scanning probe tips

Jeremy Belhassen,^{a,b} Simcha Glass,^{a,c} Eti Teblum,^d George A. Stanciu^{b,e}, Denis E. Tranca,^e Zeev Zalevsky,^{b,d,*} Stefan G. Stanciu^{b,e,*} and Avi Karsenty^{b,a,c,*}

^aJerusalem College of Technology, Lev Academic Center, Faculty of Engineering, Department of Applied Physics/Electro-Optics Engineering, Advanced Laboratory of Electro-Optics, Jerusalem, Israel

^bBar-Ilan University, Faculty of Engineering, Ramat Gan, Israel

^cNanotechnology Center for Research and Education, Lev Academic Center, Jerusalem, Israel

^dBar-Ilan University, The Nanotechnology Center, Ramat Gan, Israel

^ePolitehnica University of Bucharest, Center for Microscopy-Microanalysis and Information Processing, Bucharest, Romania

Abstract. A thorough understanding of biological species and emerging nanomaterials requires, among other efforts, their in-depth characterization through optical techniques capable of nanoresolution. Nanoscopy techniques based on tip-enhanced optical effects have gained tremendous interest over the past years, given their potential to obtain optical information with resolutions limited only by the size of a sharp probe interacting with focused light, irrespective of the illumination wavelength. Although their popularity and number of applications is rising, tip-enhanced nanoscopy (TEN) techniques still largely rely on probes that are not specifically developed for such applications, but for atomic force microscopy. This limits their potential in many regards, e.g., in terms of signal-to-noise ratio, attainable image quality, or extent of applications. We take the first steps toward next-generation TEN by demonstrating the fabrication and modeling of specialized TEN probes with known optical properties. The proposed framework is highly flexible and can be easily adjusted to be used with diverse TEN techniques, building on various concepts and phenomena, significantly augmenting their function. Probes with known optical properties could potentially enable faster and more accurate imaging via different routes, such as direct signal enhancement or facile and ultrafast optical signal modulation. We consider that the reported development can pave the way for a vast number of novel TEN imaging protocols and applications, given the many advantages that it offers.

Keywords: tip-enhanced nanoscopy; scanning probes; COMSOL simulations; nano-objects optical modeling.

Received Oct. 14, 2022; revised manuscript received Dec. 9, 2022; accepted for publication Dec. 23, 2022; published online Jan. 20, 2023.

© The Authors. Published by SPIE and CLP under a Creative Commons Attribution 4.0 International License. Distribution or reproduction of this work in whole or in part requires full attribution of the original publication, including its DOI.

[DOI: [10.1117/1.APN.2.2.026002](https://doi.org/10.1117/1.APN.2.2.026002)]

1 Introduction

Chemical and structural imaging with nanoresolution under ambient conditions is of the utmost importance for advancing our knowledge on biological processes occurring at the subcellular level,^{1–3} which in turn is needed to attain a thorough understanding of severe diseases, such as cancers and neurodegenerative or autoimmune disorders.⁴ Nanoresolution is also beneficial for understanding the operando-behavior of emerging advanced

materials⁵ or resolving interfaces in optoelectronic devices, facilitating their exploitation. Over the past decades, these applications have been the driving force for a large body of work in the field of nanoscale imaging, leading to the advent of a wide variety of techniques, each with its own strengths and limitations. Among these, fluorescence-based superresolution microscopy (f-SRM) techniques succeed in overcoming the resolution limits imposed by diffraction, reaching resolutions that range from 100 nm down to the subnanometer level.^{3,6–9} However, they still suffer from several significant drawbacks: (i) they require very specialized fluorescent probes,^{10,11} (ii) some f-SRM techniques rely on laser beam exposure levels that can lead to

*Address all correspondence to Zeev Zalevsky, zeev.zalevsky@biu.ac.il; Stefan G. Stanciu, stefan.g.stanciu@upb.ro; Avi Karsenty, karsenty@g.jct.ac.il

phototoxicity and photodamage,¹² and (iii) unpredictable anomalous processes related to the distribution of f-SRM dyes in biological samples have been shown to exist.¹³ Furthermore, due to the requirement of fluorescent labeling, their use is severely limited when it comes to resolving physicochemical properties of advanced nanomaterials or nanostructured devices that cannot be labeled.

Another family of techniques, based on tip-enhanced optical effects, has emerged over the past years as a valuable alternative that can successfully overcome the above-mentioned limitations of f-SRM. Techniques belonging to this family, such as scattering-type scanning near-field optical microscopy (s-SNOM),¹⁴ tip-enhanced Raman spectroscopy (TERS),¹⁵ tip-enhanced fluorescence (TEF),¹⁶ second-harmonic generation scanning near-field optical microscopy (SHG-SNOM),^{17,18} tip-enhanced photoluminescence,¹⁹ and photoinduced force microscopy (PiFM),²⁰ have gained tremendous interest, as they can obtain optical information at nanoscale resolution, limited only by the size of the tip used for scanning the sample, irrespective of the wavelength used for excitation.²¹ Other important features of these techniques are their ability to be used in ambient conditions, as well as their use under very low-power excitation conditions, which are not harmful to the investigated samples. Landmark experiments have shown that these techniques can be harnessed to yield resolutions, even below 1 nm.^{19,22} A major advantage of these techniques is that they share an important overlap in their architecture; they all rely on the illumination of a sharp, atomic force microscopy (AFM)-like, probe (also known as tip) that scans the surface of the sample, and on the subsequent detection of optical signals associated with the light–probe interaction. Such overlap facilitates correlative use, which is highly useful for experiments that require in-tandem access to complementary information that can be provided by such techniques.^{23–26} Approaches of this kind have great value, considering the diversity of information that can be accessed by tip-enhanced nanoscopy (TEN) techniques relying on distinct principles,²⁷ as discussed in the next paragraph.

The contrast mechanisms of s-SNOM enable mapping the dielectric properties^{28–31} and chemical composition¹⁴ of samples, which has so far facilitated a wide range of discoveries in condensed phase and two-dimensional materials.^{32–40} Additionally, s-SNOM applications in biology enable precise mapping of specific cellular and subcellular structures of interest,^{41–44} and even mapping of the exact values of important optical parameters such as the refractive index.⁴⁵ Although s-SNOM is generally acknowledged as a surface characterization technique, it nonetheless exhibits valuable capabilities for subsurface and 3D imaging.^{46–49} TERS, combining the advantages of surface-enhanced Raman spectroscopy and scanning probe microscopy technologies,^{50–52} has found utility in the investigation of a wide variety of nanostructured materials, including both organic and inorganic chemical substances. An important segment of TERS applications is the characterization of carbon materials, such as carbon nanotubes^{53–55} and grapheme,⁵⁶ as these materials are very stable during measurement and exhibit strong Raman scattering intensities.^{54,55,57,58} Although carbonaceous materials are probably the most common types of samples investigated with TERS, various biological species have also received great attention.^{15,59} Specific molecules,⁶⁰ viruses,^{61,62} bacteria,⁶³ erythrocytes,⁶⁴ membrane receptor ligands,⁶⁵ and cellular systems⁶⁶ have been studied and analyzed at the nanolevel by TERS. SHG-SNOM relies on enhancements of the SHG of either

the tip or the sample^{17,67} and is a superb tool for probing nonlinear optical properties of nanostructured surfaces or surface plasmon interactions (and their modifications), which are of importance in the context of surface-enhanced nonlinear phenomena. To give one example, SHG-SNOM has been found useful for local imaging and study of ferromagnetic and ferroelectric domains.⁶⁸ Another technique that relies on the tip–light interactions and that has brought significant added value to the TEN field is PiFM,²⁰ which has been demonstrated to be a powerful tool for probing the local polarizability of a sample at nanoscale resolutions. PiFM was shown to be highly useful for determining both linear and nonlinear⁶⁹ optical properties of materials that exhibit spatial variations on the nanoscale⁷⁰ and detectable spectroscopic contrast.⁷¹ Specific applications, such as visualizing the electric field distributions associated with propagating surface-plasmon-polaritons⁷² or identification of contaminants and defects in nanostructured materials,²⁰ imply that PiFM will play a key role in material and device characterization in the coming years. Although TEF lacks the optical sectioning capabilities of the much more popular f-SRM techniques working in the far-field regime, it remains highly relevant, as it does not require high laser beam power intensities (responsible for photobleaching and phototoxicity effects⁷³). Therefore, it can be used to investigate at nanoscale resolution any type of fluorescent sample, ranging from biological species^{74–76} (including autofluorescent ones) to nanostructured materials,^{77,78} under very simple illumination configurations that rely on unsophisticated laser sources. Its resolution outputs depend on the size of the tip and 10- to 20-nm capabilities have been demonstrated even in its earliest variants.^{16,79} An important advantage of TEF over f-SRM is that it can be easily performed in tandem with other techniques based on tip-scanning, such as s-SNOM, PiFM, and TERS, resulting in spatially and temporally co-localized information. The combination of TEF with such complementary techniques can significantly boost the in-depth understanding of fluorescent samples. For example, in a correlative imaging approach, Meng et al.⁸⁰ proposed a nanoplasmonic strategy for precision *in situ* measurements of TERS and TEF, which holds potential for becoming a popular approach for spectral analysis at nanoscale.

Although the field of TEN is constantly expanding, most imaging and spectroscopy applications reported to date rely on commercial scanning probes that are not specifically developed for TEN, but rather for AFM^{14,81,82} or for various other types of nonoptical scanning probe microscopy techniques. A consequence of this is that the optical properties of these tips are not provided by the manufacturers, as they are irrelevant to the applications they natively target. This issue is exacerbated by the fact that important properties, such as absorption, scattering, and reflectance are difficult to experimentally measure for objects at the scale of scanning probe tips. In this work, we propose an approach for TEN, where techniques such as those mentioned above, harness the versatility, potential, and performance of tips that are specifically designed and manufactured for applications in nanoscale tip-enhanced optical imaging. To this end, we propose a framework based on COMSOL simulations⁸³ and nanomanufacturing that represents a solution for developing specialized tips for TEN, with well-understood and tailorable optical properties. This follows up on recent related endeavors, which have demonstrated the very high potential of TEN imaging with application customized probes.^{19,84} We provide a proof-of-concept example, in which we design and

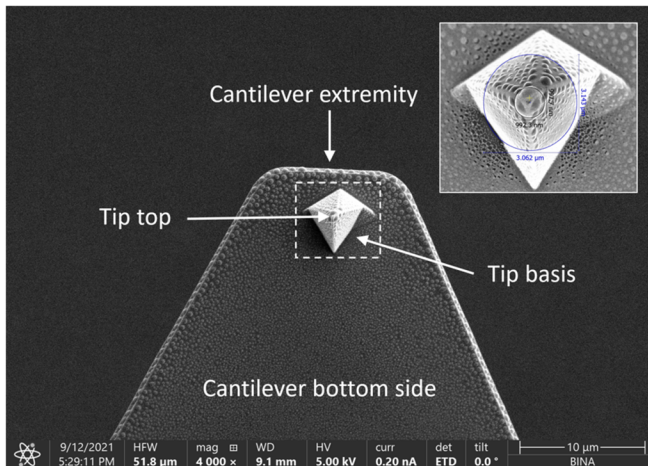
fabricate two variants of silicon scanning probe tips featuring Au NPs on their apex, whose optical properties we approximate by numerical simulations. Although previous efforts successfully demonstrated, in the context of other applications, scanning probe tips with various attached NPs,^{85–87} to the best of our knowledge, assessing or modeling the optical properties of these constructs was never in question until now. We argue that the optically resolved probes that we propose can be useful in enabling nanoscopy applications that exploit in a well-understood manner the plasmon energy transfer occurring between the excited tip and the investigated samples. This can potentially enable higher signal-to-noise ratio (SNR) either by direct mechanisms for background suppression or via indirect mechanisms based on ultrafast and precise modulation of the tip's near field. Furthermore, tuning the illumination wavelength to achieve different scattering profiles from the tip, in a well understood manner, can potentially be used to enable various signal modulation strategies tailored for near-field techniques whose contrast is intertwined with the tip's scattering. Additionally, precise

knowledge on the tip's absorption and scattering properties holds great potential for optimizing existing nanolithography methods based on tip illumination and for enabling novel, and highly efficient, tip-enhanced ablation/writing schemes. In the next sections, we describe our tip fabrication and modeling methodology, present our results, and provide a series of discussions on potential utility and applications.

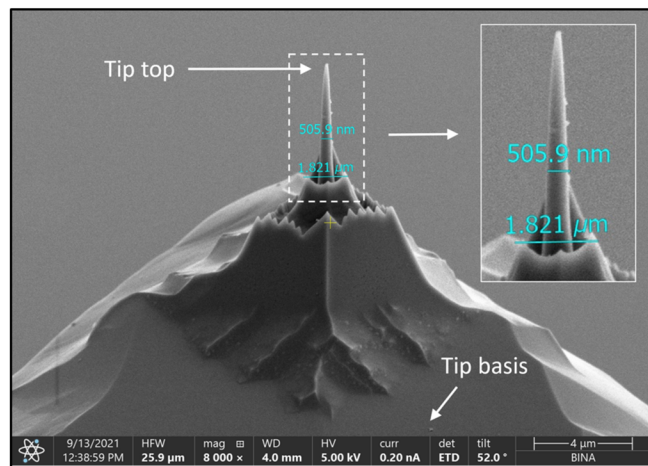
2 Methods

2.1 Tip-Fabrication Methodology

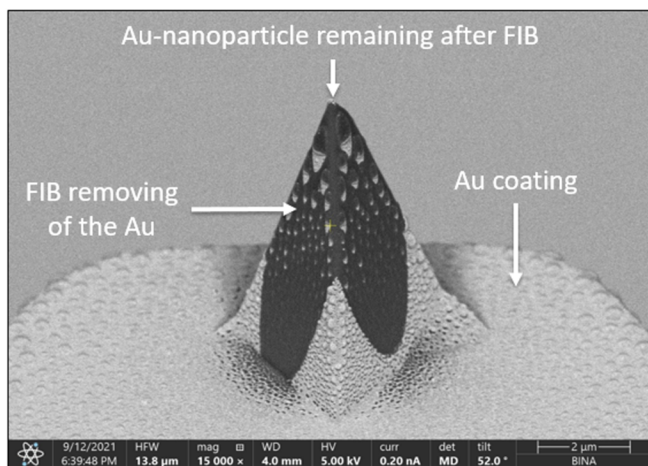
Two custom-modified probes were fabricated, based on commercially available ones. We opted for silicon probes that do not present plasmon effects overlapping with those of the plasmonically active material that we employed (Au). Using such probes as foundation for this framework results in a simple and reproducible fabrication process. In Fig. 1, scanning electron microscope (SEM) pictures of the two AFM tips, NP-S10 (Bruker) [Fig. 1(a)] and TESP-HAR (Bruker) [Fig. 1(b)], can be



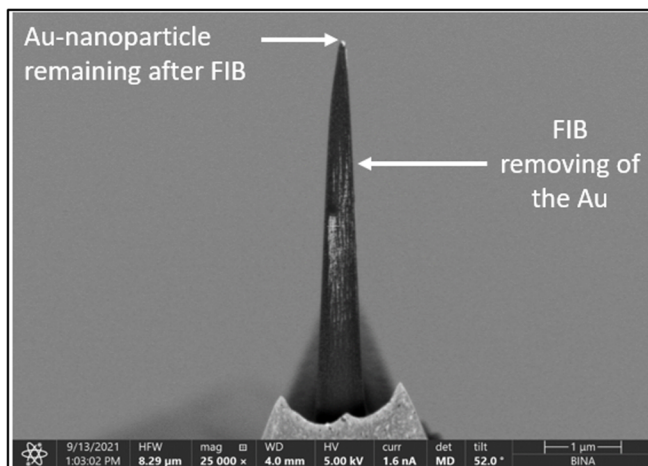
(a)



(b)



(c)



(d)

Fig. 1 SEM micrographs of the commercial AFM probes before and after custom processing: (a) NP-S10 probe (bottom view); (b) TESP-HAR probe (side view); (c) NP-S10 probe after Au thin-film deposition and subsequent FIB processing; FIB removal of the Au thin film can be observed; (d) TESP-HAR probe after Au thin-film deposition and subsequent FIB processing.

observed. These were modified in two steps [Figs. 1(c) and 1(d)] so that an Au NP is positioned on their apex. The tips were first coated with a 10-nm-thick Au layer by sputter deposition. Afterward, the Au layer was removed by focused ion beam (FIB)^{88,89} sputtering over the whole tip excepting the apex, resulting in an Au nanoparticle (NP) remaining there. In Figs. 1(c) and 1(d), one can observe the last step of the tip fabrication.

2.2 COMSOL Simulations Methodology

2.2.1 Half-sphere and cylinder models

The physical parameters of interest in this experiment are the probe's plasmon band and its size. Although experimental measurements of the scattering and absorption spectrum of the probe could potentially be used to assess its plasmon band, such results are very difficult to obtain on nanosized objects. However, numerical analysis does not suffer from this limitation. Moreover, as recently shown in other works on TEN imaging, simulation methods allow for the testing of different tip geometries and sizes so as to identify their influence on the imaging outputs.⁹⁰ As discussed further in this section, to fabricate TEN probes with known optical properties, we adopted a fabrication approach whose final result is the deposition of an Au NP of custom size on the apex of a commercial AFM probe. Two commercial AFM probes with distinct geometries were considered, NP-S10 (Bruker) and TESP-HAR (Bruker).

In Fig. 2(a), an SEM image of the apex of one of the custom-modified probes is presented, with the Au NP clearly noticeable at the extremity of the tip. Since we have used a probe substrate (Si) that is plasmonically inactive in the spectral region matching the plasmon band of the Au NP, any potential plasmon resonance energy transfer (PRET) occurring between the tip and the sample will be governed by the optical properties of the Au NP alone. It follows that it suffices to model only the NP in our COMSOL simulations. In addition, although the fabrication process discussed earlier results in an ellipsoidal-shaped NP, we assume that it can be accurately modeled as either

a half-sphere [Fig. 2(b)] or a thin cylinder [Fig. 2(c)], both of radius R .

The radii of the NP models used in the COMSOL simulations were determined by measurements performed on the actual particles after the fabrication procedure. The radii were found to lie in the following ranges.

- For the NP-S10-based tip: $129.5 \text{ nm} < 2R < 153.8 \text{ nm}$.
- For the TESP-HAR-based tip: $70.15 \text{ nm} < 2R < 75.54 \text{ nm}$.

The initial radii of curvature of the two considered probes were 20 and 10 nm for the NP-S10 and TESP-HAR probes, respectively.

2.2.2 Model implementation in COMSOL

In Fig. 3, we present the geometry of our COMSOL simulation for the case of the hemispherically approximated NP. Given the high computational time required for 3D finite-element method simulations, only half of the NP was modeled; symmetry lets us extrapolate the results to the entire structure. (This methodology was inspired by a COMSOL Applications Library example on Mie scattering that addressed structures of a similar kind.) One can discern three different layers in the representation of the model. The outer one is a perfectly matched layer (PML), used to simulate open boundaries⁹¹ by absorbing the outgoing electromagnetic waves and canceling spurious reflections; the middle one models the ambient air around the NP; and the inner one models the NP itself. The illumination is simulated as electromagnetic plane waves propagating along the x axis. The measurement of the scattering and absorption was performed by integration over the entire external interface of the air layer. The simulation concept for the cylinder shape model is defined along similar lines.

2.3 Resonance Characterization Methodology

To measure the effective plasmon resonance of the probes, a challenging series of measurements of the light spectrum scattered from the tip were performed by means of a spectrometer

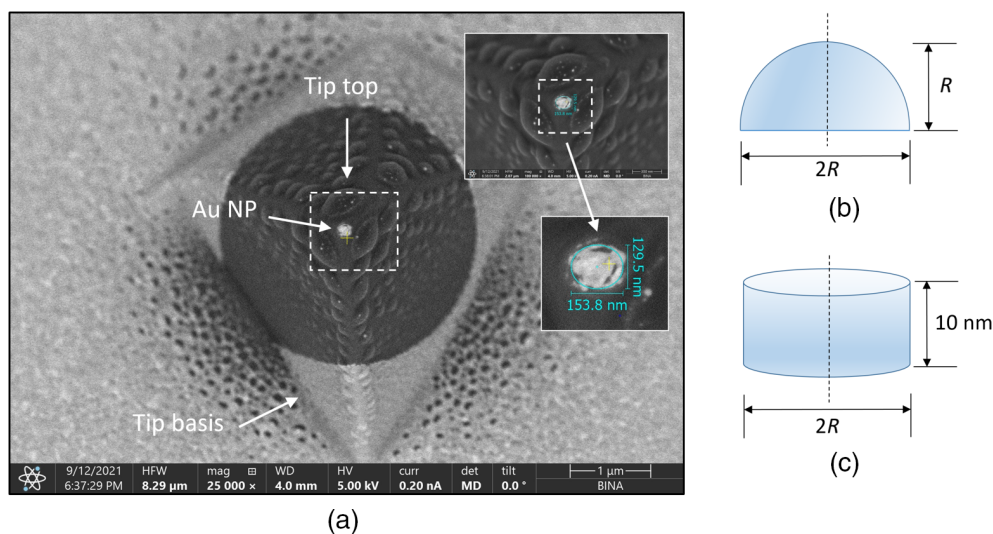


Fig. 2 (a) SEM image of the custom-modified probe (NP-S10): AFM silicon tip with an Au NP at its apex. One can assume a circular shape of this NP, with radius R . Diagram of (b) half-sphere and (c) thin cylinder models by which the NP can be approximated.

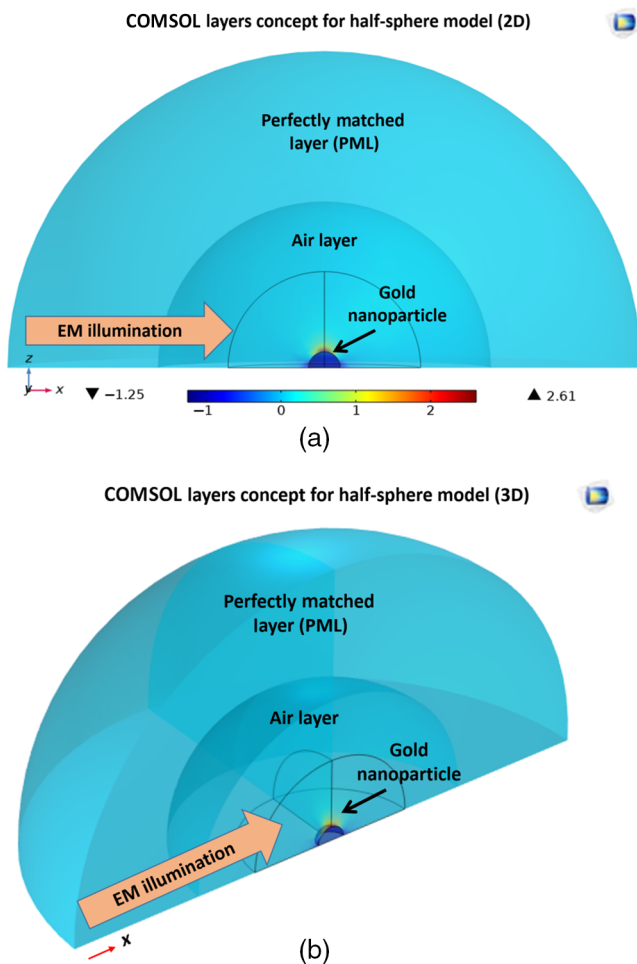


Fig. 3 COMSOL geometry models: (a) 2D layers and (b) 3D layers concepts for the half-sphere model. The geometry is divided in three layers: PML, air, and Au NP. In this specific case, the illumination of the sphere is considered along the x axis, while the relative electric field is along the z axis.

connected to fiber optics. The scattering from the tip was obtained via dark-field microscopy using a Carl Zeiss Axiotron optical microscope, and a ThorLabs Compact Spectrometer 350 to 700 nm was connected to the system and used for the resonance measurements. Figure 4 presents various images of the cantilever and tip characterization under bright- and dark-field microscopy. Figure 4 shows the experimental characterization system configuration. Figure 4(a) presents the fabricated NP on the top of the tip, using an SEM. By means of this configuration, spectra were obtained and compared for several intensities [Fig. 4(c)]. The last step consisted in a screening analysis in order to identify the plasmon resonance wavelength [Fig. 4(d)].

2.4 Description of the Setup Used for Validating the AFM Function of the Processed Probes

Atomic force microscopy (AFM) measurements were carried out using a Bio FastScan scanning probe microscope (Bruker AXS). All images were obtained under tapping mode operation with the nonprocessed TESP-HAR and processed TESP-HAR-

Au probes. The measurements were performed under environmental conditions in an acoustic hood to minimize the vibrational noise. The images were captured in the retrace direction with a scan rate of 1.0 Hz. The resolution of the images was 256 samples/line. For the image processing and analysis, we used Nanoscope Analysis software. The “flating” and “plane-fit” functions were applied to each image.

3 Results

3.1 Au Apex Shapes and Measured Dimensions

As discussed in the introduction, the purpose of this experiment is to demonstrate the viability of combining nanofabrication and numerical simulation in the manufacture of custom TEN probes. We previously detailed the two-stage process through which commercial grade probes were modified to equip their apex with Au NPs (first sputter deposition and then FIB removal); here we present the results of that process. One can observe the dimensions of the Au NPs that resulted for the NP-S10 and TESP-HAR probes in Figs. 5(a) and 5(b), respectively. For the NP-S10 probe, the smallest NP obtained (dictated by the maximum FIB resolution) was of ellipsoidal shape, with axes of 129.5 and 153.8 nm, and therefore, an eccentricity of 0.54. For the TESP-HAR probe, the smallest Au NP obtained was also of ellipsoidal shape, with axes of 70.15 and 75.54 nm and an eccentricity of 0.27. Figures 5(c) and 5(d) present top views of the different existing diameters from the bottom of the tip to its top.

3.2 Numerical Results

3.2.1 COMSOL simulation results for the half-sphere model

In Fig. 6, we present our simulations of the scattering [Figs. 6(a) and 6(c)] and absorption [Figs. 6(b) and 6(d)] cross sections as a function of the wavelength for the half-sphere model. Different radii R (Fig. 2) were simulated in a range of sizes close to the dimensions of the fabricated tips. Since in reality the NP exhibits an ellipsoidal shape, the radii tested were chosen to be in the range between the sizes of the semiminor and semimajor axes. We assume that the properties of the real tips are close in value to the results numerically simulated for the considered range of R . Table 1 shows the value of the scattering and absorption cross sections' maxima as a function of the radius.

For a radius R , corresponding to the ellipsoidal NP of the NPS-10, one can observe the following. First, for all the considered radii, a local maximum of the scattering is observed between 555 and 590 nm (see also Table 1). These values are close to 532 and 561 nm, two wavelengths that are commonly used for fluorescence microscopy,^{92,93} an aspect that can potentially be used in TEF applications building on PRET. Second, the wavelength corresponding to the resonance of the scattering increases with the NP radius. Concerning the absorption cross section, for all the different radii, the maxima are observed between 500 and 514 nm (see Table 1). In Figs. 6(c) and 6(d), we present the simulated scattering and absorption cross sections, respectively, for the considered radii range corresponding to the ellipsoidal NP of the TESP-HAR probe. The scattering cross sections' maxima were obtained in the range from 522 to 526 nm, whereas the absorption cross sections' maxima were obtained in the range from 512 to 514 nm.

According to the quasistatic approximation, the scattering and absorption maxima have to match. The corresponding

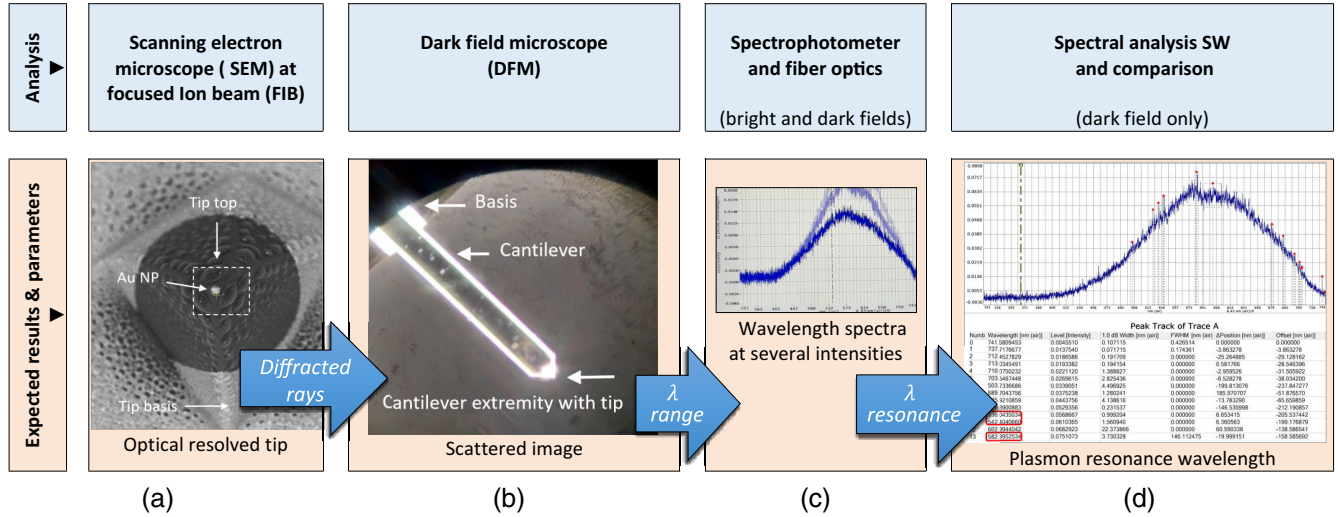


Fig. 4 Characterization workflow: (a) SEM analysis of the NP at the top of the tip; (b) cantilever extremity under dark-field; (c) spectra under bright and dark-field modes; and (d) experimental system configuration. Incident white light illuminates the optically resolved tip. The tip extremity is then observed using a dark-field objective lens, so the scattered light is filtered and observed. The scattered light is then split into two paths: the first one is used for optical imaging through the camera, and the second one is used for spectrometry analysis aimed at detecting the positions of the resonance peaks.

scattering and absorption cross sections of a sphere of radius a , calculated via the Poynting vector, from the full electromagnetic (EM) field associated with an oscillating dipole are defined by the following set of equations.⁹⁴ The expression of the scattering cross section is given by the following equation:

$$\sigma_{\text{sca}} = \frac{k^4}{6\pi} |\alpha|^2 = \frac{8\pi}{3} k^4 a^6 \left| \frac{\varepsilon(\omega) - \varepsilon_d}{\varepsilon(\omega) + 2\varepsilon_d} \right|^2. \quad (1)$$

The absorption cross section can be expressed by the following equation:

$$\sigma_{\text{abs}} = k \text{Im}(\alpha) = 4\pi k a^3 \text{Im} \left[\frac{\varepsilon(\omega) - \varepsilon_d}{\varepsilon(\omega) + 2\varepsilon_d} \right]. \quad (2)$$

The total cross section is given by the following equation:

$$\sigma_{\text{ext}} = \sigma_{\text{sca}} + \sigma_{\text{abs}}, \quad (3)$$

where the coefficient α is equal to $4\pi a^3 \frac{\varepsilon(\omega) - \varepsilon_d}{\varepsilon(\omega) + 2\varepsilon_d}$, ω is the frequency of the planar wave illumination, ε is the permittivity of the Au NP, and ε_d is the permittivity of the dielectric (air).

The resonance is obtained at the Fröhlich condition [Eq. (4)],

$$R_e[\varepsilon(\omega)] = -2\varepsilon_d. \quad (4)$$

The quasistatic approximation is justified for particles that are smaller than the wavelength, which is typically the case for particles of a dimension of 100 nm and less.⁹⁴ Since the presented NPs range in size from 60 to 180 nm, some of them can be described using such an approximation.

In case of a large NP, the corresponding scattering and absorption cross sections will become Eqs. (5) and (6), respectively,

$$\sigma_{\text{sca}} = \frac{2\pi}{k^2} \sum_{n=1}^{\infty} (2n+1) (|a_n|^2 + |b_n|^2), \quad (5)$$

and

$$\sigma_{\text{abs}} = \frac{2\pi}{k^2} \sum_{n=1}^{\infty} (2n+1) \text{Re}(a_n + b_n), \quad (6)$$

so we get

$$\sigma_{\text{abs}} = \sigma_{\text{ext}} - \sigma_{\text{sca}}. \quad (7)$$

In such a case, the corresponding cross sections are still calculated via the Mie theory, whereas the electrostatic approximation breaks down, and the retardation effects must, therefore, be considered. In the case of PRET,⁹⁵ a process that can influence tip-sample interactions accounting for TEN contrast (e.g., in tip-enhanced fluorescence), the energy absorbed by the tip via plasmon excitation is transferred to the sample. In this case, the absorption cross section is more relevant than the scattering cross section. In the case of s-SNOM, the scattered field comprises a series of terms,⁹⁶ namely, the incident field (i) scattered by the tip, (ii) scattered by the sample, (iii) scattered by the sample and then by the tip, (iv) scattered by the tip and then by the sample, and (v) scattered by the tip, then the sample, and finally the tip again. The sample properties dictate the weight of each of these terms in the recorded signals, but for an s-SNOM configuration based on detection at higher harmonics of the tip's oscillation frequency, the incident field scattered by the sample should be discarded.⁹⁶ Thus considering that the scattering by the tip is mainly responsible for the s-SNOM attainable contrast, in potential s-SNOM applications with optically resolved probes, the scattering cross section may be more relevant than the absorption cross section. In nanolithography⁹⁷ and ablation⁹⁸

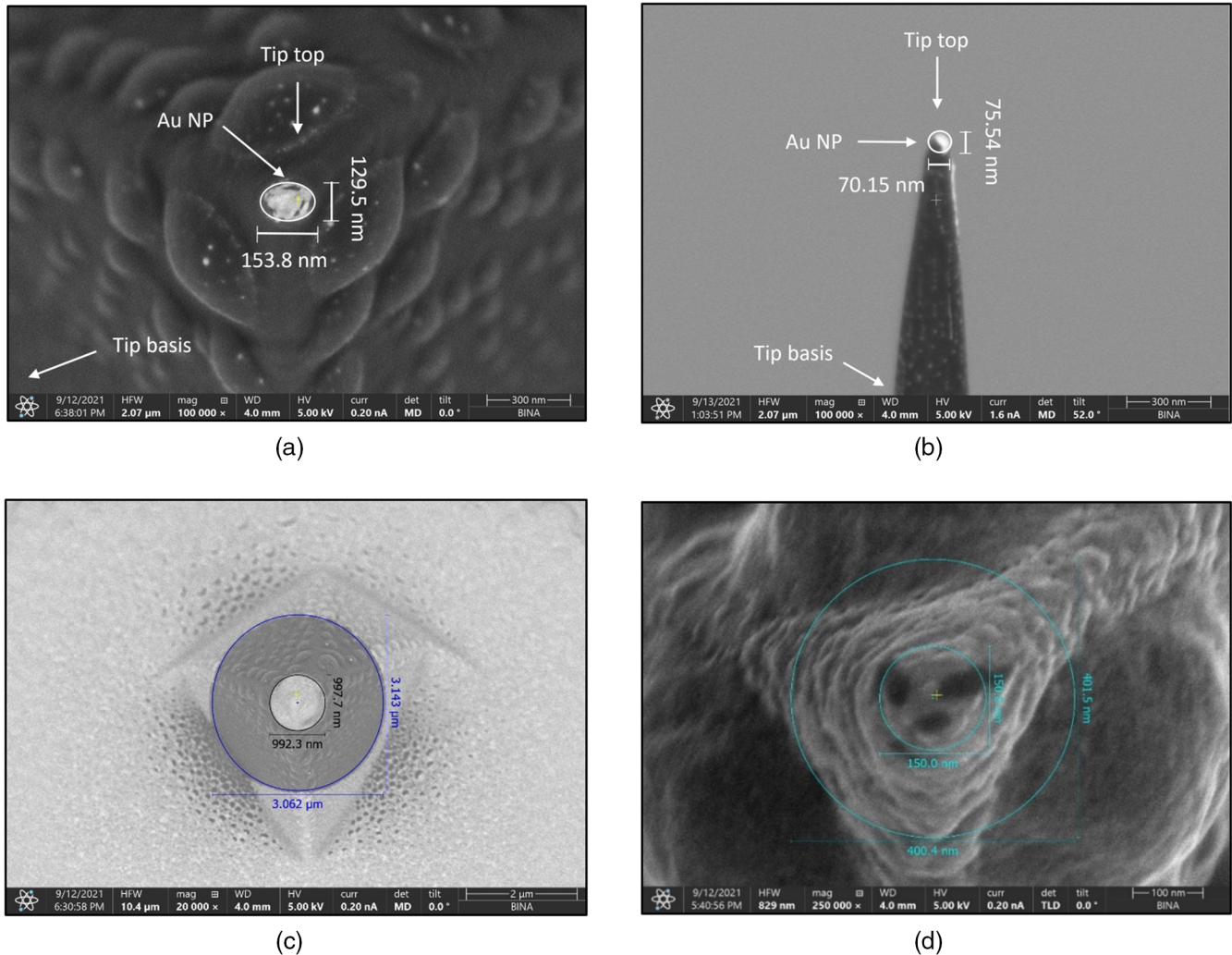


Fig. 5 SEM pictures of the custom-modified tips. Au NPs can be observed on the apex of the probes. (a) NP-S10 probe; (b) TESP-HAR probe; (c) top view of the diameters starting from the basis of the tip (μm) and up toward upper stages of the tip (nm); and (d) zoom-in of the top view. Dimensions of the Au NPs are presented in (a) and (b).

approaches based on tip-enhanced illumination, both the scattering and absorption cross sections can be equally important for optimizing the final outputs, depending on the specifics of the application at hand.

3.2.2 COMSOL simulation results for the cylinder model

In Fig. 7, we present the simulated scattering and absorption cross sections as a function of the wavelength for the cylinder model. For a radius R corresponding to the ellipsoidal NP of the NPS-10, the following phenomena can be observed for the scattering [Fig. 7(a)] and absorption [Fig. 7(b)] cross sections: first, for all the different radii, a local maximum of the scattering phenomenon is observed between 522 and 530 nm. However, contrary to the half-sphere model results, one can notice that the wavelength corresponding to the resonance of the scattering seems here to decrease with the radius. In regard to the absorption cross section, for all the different radii, the maxima are observed between 500 and 504 nm. The scattering and absorption cross section results for the NP deposited on the apex of the TESP-HAR are presented in Figs. 7(c) and 7(d), respectively.

In this case, the maxima of the scattering cross sections are localized between 530 and 534 nm, whereas the absorption cross sections' maxima are localized between 508 and 518 nm. The value of the scattering and absorption cross sections' maxima is summarized in Table 2 as a function of the NP radius.

3.3 Characterization Results

3.3.1 Bright field versus dark field

To enable clear identification of the plasmon response, after checking the tip in bright-field mode [Fig. 4(a)], it was necessary to illuminate the cantilever and the tip in dark-field mode [Figs. 4(b) and 4(c)]. Several challenges arose in the effort to illuminate the tip. First, even if the illumination is off, the background illumination resulting from the scattering due to the edges of the silicon cantilever still has influence on the spectrum. Thus, while trying to isolate the resonance peak from the extremity of the Au NP, one can assume that the additional spectral responses are obtained from the rest of the probe, also covered by a metal layer. This is why it is not straightforward to

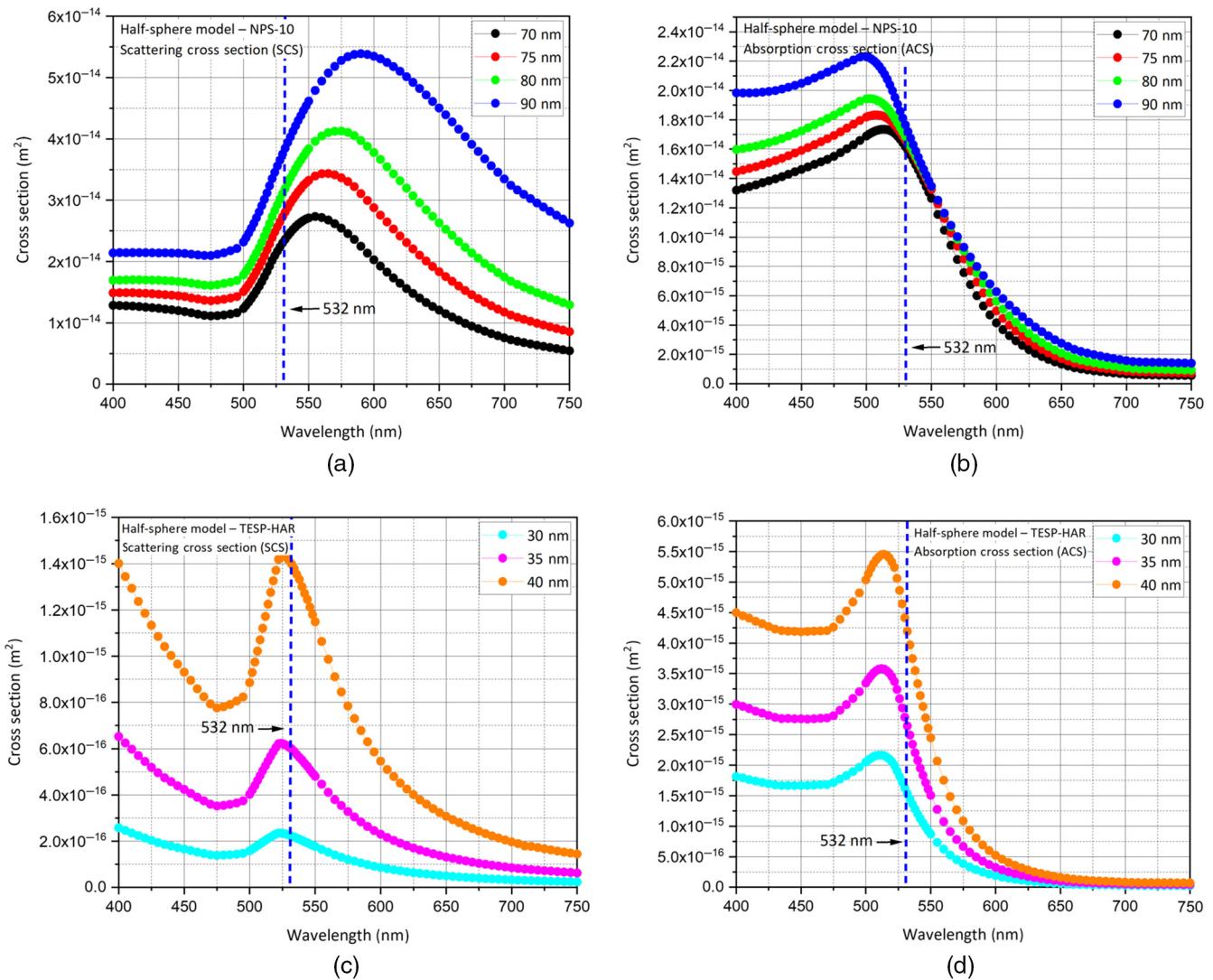


Fig. 6 COMSOL results on the scattering and absorption cross sections using the half-sphere model. For NPs of different radii deposited on the apex of the NP-S10 probe: graphs of the (a) scattering and (b) absorption. For NPs of different radii deposited on the apex of the TESP-HAR based tip: graphs of the (c) scattering and (d) absorption.

Table 1 Wavelengths of the maximum scattering and absorption for Au NPs with radii of different sizes, calculated by approximating the tip shape with the half-sphere model.

Radius (nm)	30	35	40	70	75	80	90
Scattering (nm)	522	524	526	555	565	575	590
Absorption (nm)	512	512	514	514	508	502	500

measure the optical properties of individual small objects placed in proximity of other structures, and some gaps may appear compared to the simulations, where one can isolate an illuminated surface with high accuracy, and the measured spectrum obtained through the whole system.

3.3.2 Spectrometer curves

Although numerical results (also known as COMSOL simulations) presented a forecast of the tips' expected behavior,

experimental results became necessary to confirm and analyze the scattering and the absorption phenomena. As per previous works, based on Mie theory, it appeared that for highly doped Si NPs (known to act as a metal), the resonance frequency increases with the size of the NP.⁹⁹ Similar conclusions were obtained with silver NPs sharing different sizes.¹⁰⁰ Dark-field optical microscopy can be used to detect plasmon resonance of a single particle, since the dark-field condenser acts like a filter for the directly transmitted light, whereas only the

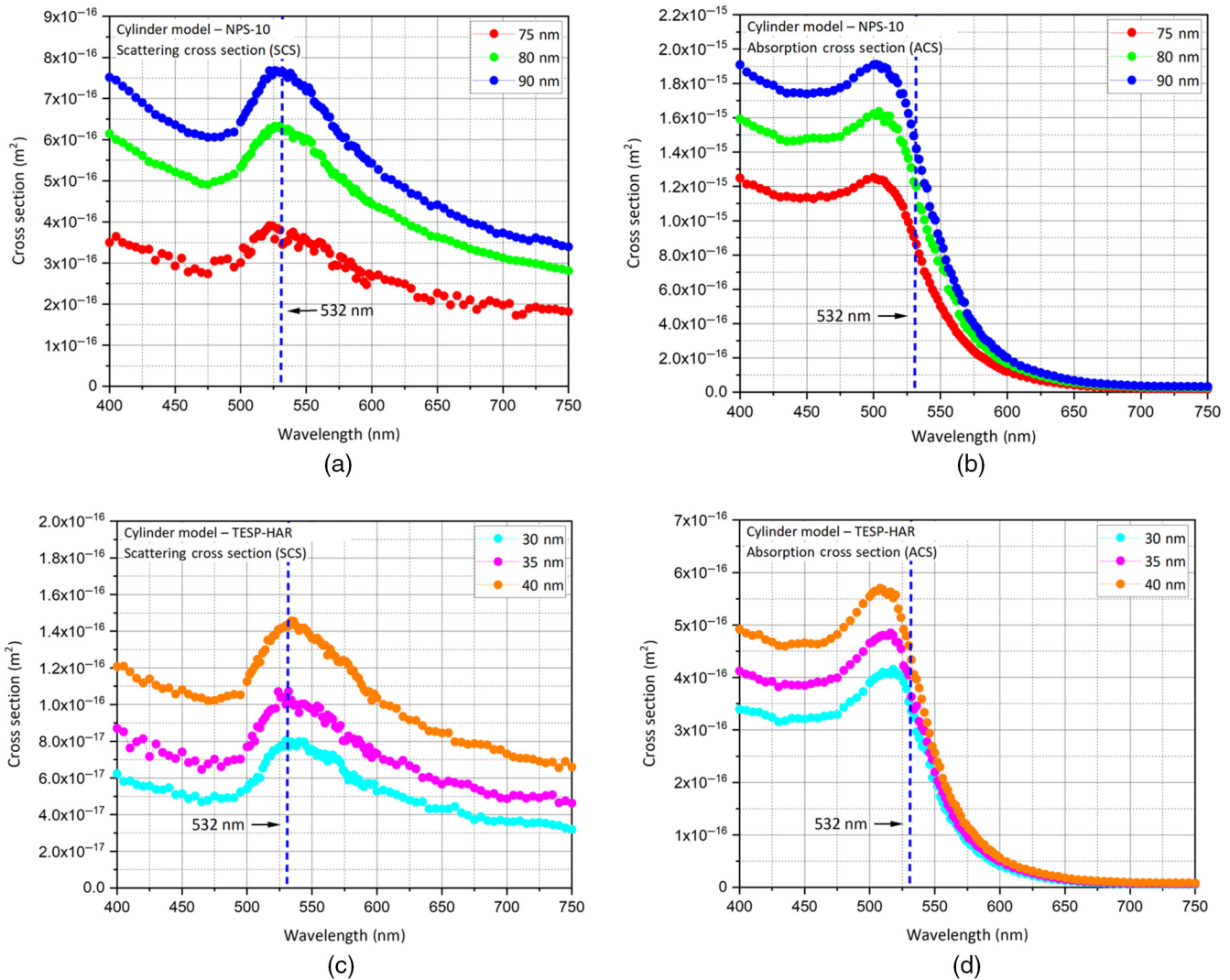


Fig. 7 COMSOL results on the scattering and absorption cross sections using the cylinder model. For NPs of different radii deposited on the apex of the NP-S10 probe: graphs of the (a) scattering and (b) absorption. Since for NPs with radii of 70 and 75 nm, the curves are fully matched; we present only the results for the 75 nm NP. For NPs of different radii deposited on the apex of the NP-S10 TESP-HAR probe: graphs of the (c) scattering and (d) absorption.

Table 2 Wavelengths of the maximum scattering and absorption for Au NPs with radii of different sizes, calculated by approximating the tip shape with the cylinder model.

Radius (nm)	30	35	40	75	80	90
Scattering (nm)	530	532	534	522	530	524
Absorption (nm)	518	516	508	500	504	502

scattered light is observed.⁹⁴ Since plasmon resonance leads to scattering maximum [Eqs. (1) and (5)], the effect of incident white light is studied to find in which visible wavelength the resonance occurs. The scattered light is then analyzed by spectrometry analysis. Figure 8 presents a series of measured spectra, recorded while illuminating the tips in bright- and dark-field modes. At this stage, it appeared that the most promising type of

tip, toward future optically resolved scanning probes, was the TESP-HAR model, given the higher consistency of the obtained results. Indeed, the resonance wavelength, obtained by the performed simulation, matches the common 532 nm illumination wavelength, which can be desired in practical applications (as shown in Fig. 7 and Table 2). Regarding the fabricated probes, Fig. 8(a) presents the measured spectrum in bright-field mode.

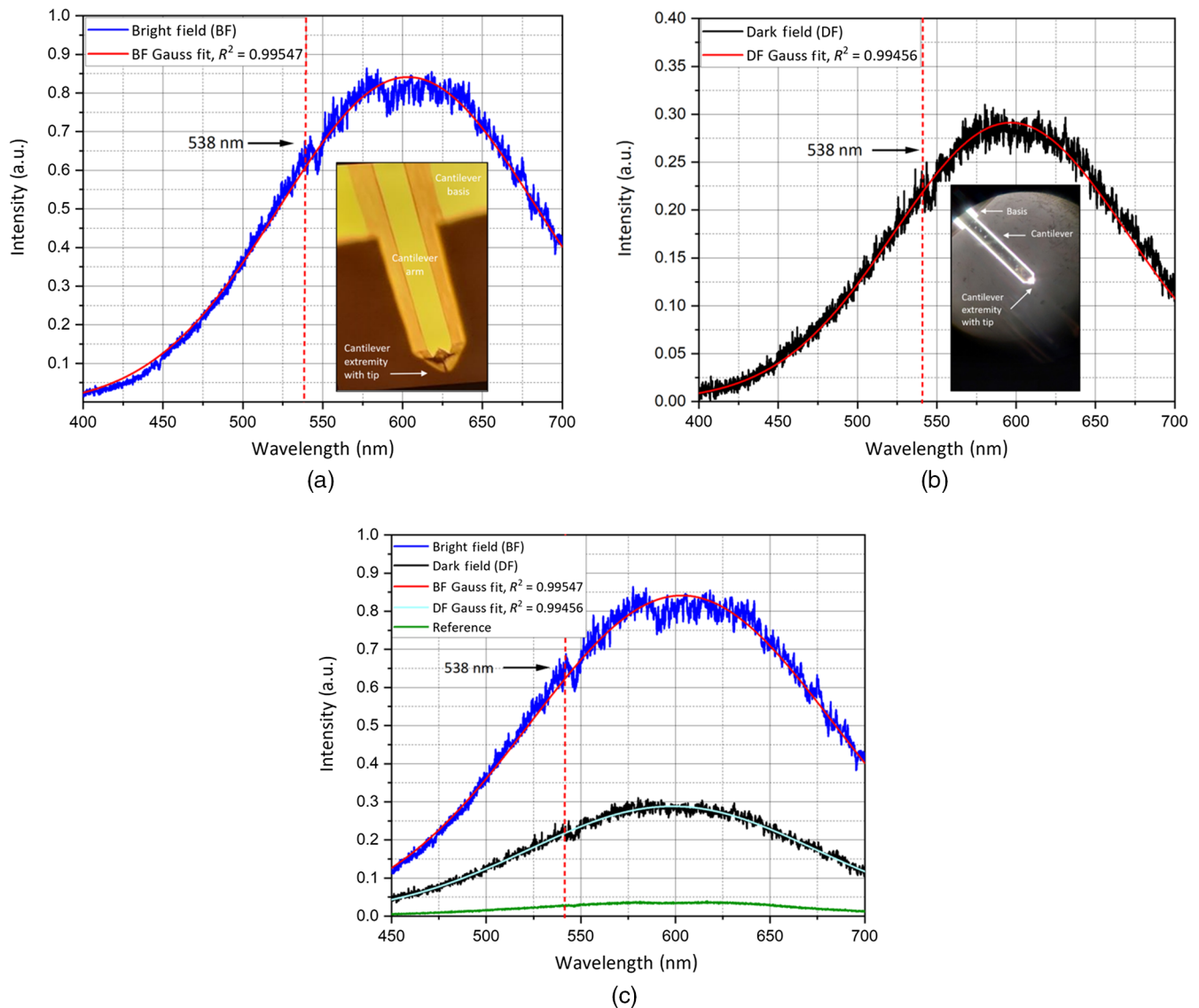


Fig. 8 Spectrometer measurements of the resonance wavelength. (a) Bright-field mode, magnification $M = 150\times$, and integration time $t = 900$ ms. (b) Dark-field mode, magnification $M = 50\times$, and integration time $t = 900$ ms. (c) Comparison of bright field, dark field, and reference spectra.

A resonance peak can be observed at 538 nm. Figure 8(b) presents the measured spectrum in dark-field mode. Although dimmer, the resonance peak at 538 nm can still be observed. It should be noted that the measured intensity in the dark-field mode is almost one-third when compared to the bright-field mode's intensity, for the same integration time of 900 ms.

3.4 Validation of AFM Function of the Processed Tips

Although showcasing advantages of the proposed tips and of the associated optical modeling framework will be addressed in dedicated follow-up work, we present next a series of results that demonstrate the unaltered AFM function of the processed probes.

To demonstrate the unaltered capabilities for topographic imaging of the modified probes, we performed tapping-mode AFM on several types of samples, such as nanoantenna and

nanospheres with the commercial, nonprocessed, TESP-HAR probes and with the modified instances, TESP-HAR-Au. Similar results (not shown here) were obtained for the NP-S10 probes. Figure 9 presents the main results of the scanning experiments performed on the following.

1. A VGRP-15M platinum (Pt) coated reference sample with square wells, exhibiting a width of $5.6 \mu\text{m}$, a pitch of $10 \mu\text{m}$, and a depth of 180 nm , as presented in Figs. 9(a) and 9(d).
2. A series of Au spherical NPs of 260 nm average diameter deposited on a $10 \mu\text{m} \times 10 \mu\text{m}$ flat surface, as presented in Figs. 9(b) and 9(e).
3. A single Au spherical NP on a flat surface, exhibiting a diameter of 263 nm and a height of 129 nm , as presented in Figs. 9(c) and 9(f).

The unaltered AFM function of the processed tips can be best observed based on the three topographic profiles recorded with

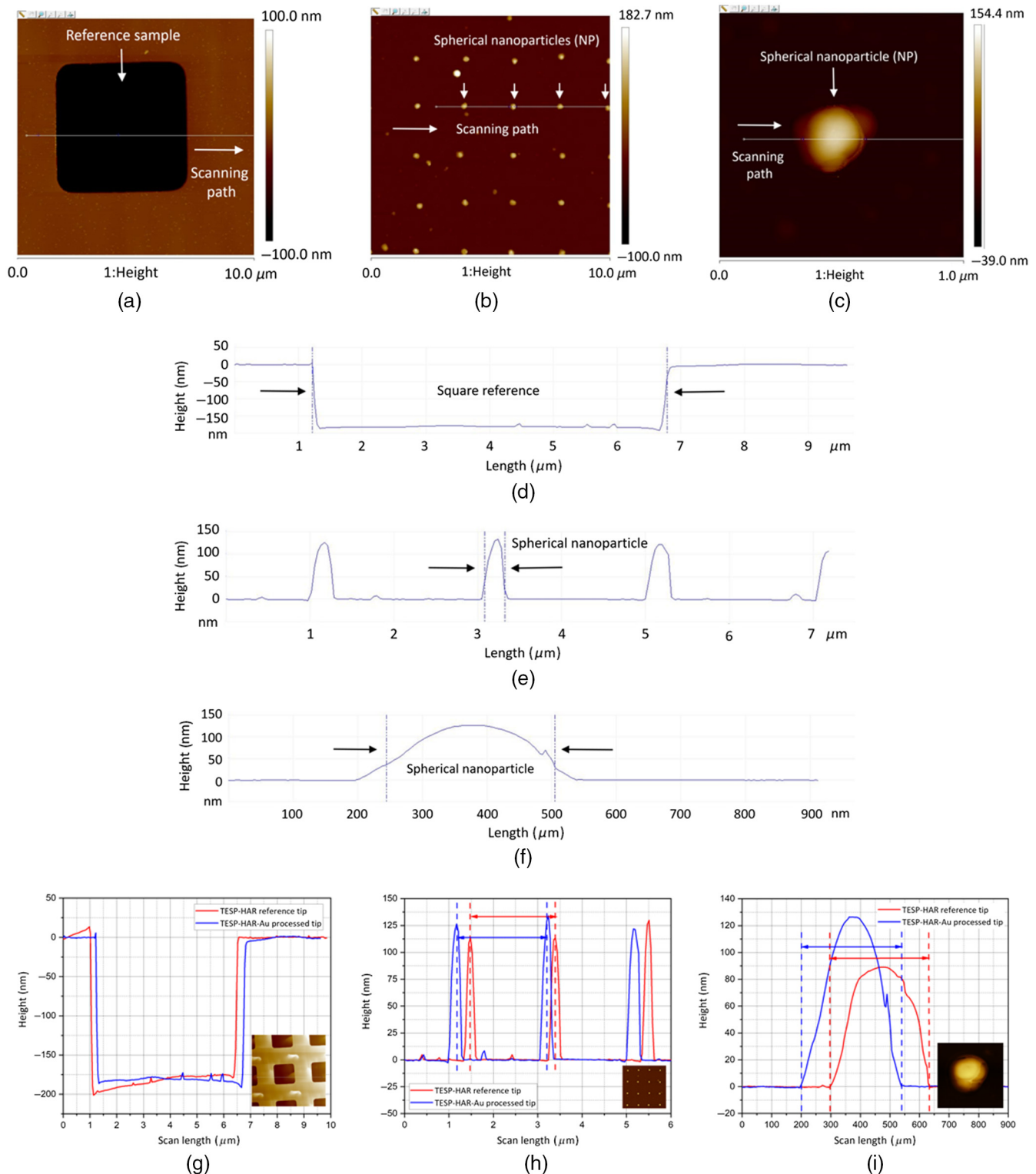


Fig. 9 Validation of AFM function by comparing the tapping-mode topographic outputs of the processed TESP-HAR-Au tip versus the commercial nonprocessed TESP-HAR tip. AFM imaging of (a) VGRP-15M platinum (Pt)-coated reference sample, (b) series of Au spherical NPs, and (c) single Au spherical NP. Topography curves along the white profile line for (d) VGRP-15M platinum (Pt)-coated reference sample, (e) series of Au spherical NPs, and (f) single Au spherical NP. Scan comparison results on (g) VGRP-15M sample, (h) spherical NPs sample, and (i) single spherical NP sample.

both nonprocessed and processed tips, TESP-HAR and TESP-HAR-Au. Although tiny amplitude and phase shifts between the two measured curves are noticeable, the results obtained for both tips are similar, which means that in spite of the processing the TESP-HAR-Au maintains its AFM capability. The differences between the curves can be explained by several aspects that do not affect the validity of the successful concept. First, the addition of an NP at the end of a tip can affect the diameter of its apex. By processing according to the proposed methodology, the diameter of a commercial AFM tip will increase by few tens of nanometers. Such a change will not affect the accuracy on long scans, as presented in Figs. 9(g) and 9(h), where the amplitudes are similar for both TESP-HAR and TESP-HAR-Au. However, it can affect the scans of objects of smaller dimensions, as presented in Fig. 9(i). An additional explanation of the noticeable phase shifts is purely related to a small registration mismatch between the positions of the profile lines with respect to the sample surface. This experiment has been done manually and bringing the two scan curves on the same graph was intended for proof-of-concept comparison, to show that the processed tip kept its capability to scan; therefore, precise and nanometer-level registration was not intended.

4 Discussion

At present, although TEN imaging has enabled important discoveries, the outputs of these techniques are largely biased by the use of nonspecialized probes. Here we propose the idea of using optically resolved probes, which can potentially significantly augment nanoscale imaging with TEN, by enabling routes for a higher SNR, and consequently, higher resolution and faster acquisition rates. We showed that by coating a commercial AFM probe with a thin layer of Au, and then processing it by FIB, an Au NP can be placed on its apex. By experimenting with two very different probes, we demonstrated that this methodology can be implemented irrespective of the tip's geometry. Other materials besides Au, such as Pt, Cr, and Ag, could also be used, depending on the tip properties required by specific applications. Alternative approaches, not demonstrated here, could consist in attaching NPs of known size and shape to tipless cantilevers, but according to our past experiences on the topic, such approaches can be significantly more challenging. Furthermore, such approaches would result in probes with peculiar tip-shanks, whereas the current body of understanding on near-field data⁹⁰ incorporates the specific geometries of traditional AFM tips, which the methodology proposed here better maintains. Further on, we showed that by COMSOL numerical simulations we can approximate the optical properties of the NP resulting on the probe apex after FIB processing. Experimental assays based on bright-field and dark-field microscopy and spectroscopy can be eventually implemented to validate the numerical results. We consider that the proposed framework could result in the advent of TEN imaging approaches where investigations are done with specialized tips whose known optical properties can be exploited for better and faster investigations. To this end, in the next paragraph, we discuss two potential applications.

TEF implementations that rely on the coupling between the absorption band of fluorophore and localized surface plasmon resonance of the tip-substrate system,^{16,101,102} hold important potential to resolve many of the typical drawbacks of more simplistic TEF imaging approaches, where the properties of the probe are not thoroughly taken into account,^{74–76} such as low

SNR and intrinsic high acquisition time. In traditional tip-enhanced fluorescence microscopy, all fluorophores under the influence of the laser beam tuned to the absorption band of the fluorophore beam emit light. The light emitted by a single fluorescent particle (or by a cluster of reduced size) is modulated by vertically oscillating a metallic tip on top of it and extracted with a lock-in amplifier [Fig. 10(a)]. Intense background accounts for severe drawbacks such low SNR, and consequently low acquisition time, which hinders the popularity of such imaging approaches, despite their valuable potential for ultrahigh resolution. In an alternative approach that can potentially overcome these drawbacks, the fluorophores are excited via the PRET^{95,103} from a tip that is illuminated with a wavelength promoting surface plasmon resonances within it. This can lead to a significant suppression of background signals, as the fluorophores close to the excited one do not benefit from the PRET effect [Fig. 10(a)]. Implementing this imaging modality requires that the plasmon band of the tip and the absorption band of the probed fluorescent molecules overlap⁹⁵ [Fig. 10(b)]. However, the plasmon band of commercial AFM probes is not explicitly provided by manufacturers nor can it be easily measured; thus, approaches as those described above can currently be implemented based on trial-and-error approaches, which is impractical. Our results demonstrate the valuable synergy between a numerical simulation framework and a nanofabrication methodology, which can be used to obtain tips with known plasmon band, which are highly suitable for the above-described application. Specifically, the developed tips have a well-defined absorption band, with absorption cross section's maxima ranging between 500 and 518 nm, depending on the size of the NP resulted on the tip apex after FIB processing (Tables 1 and 2), as was assessed by numerical simulations. By tuning the illumination to the simulated absorption band leads to local surface plasmon resonances in the tip apex, which can be transferred to the sample via a PRET effect, supposing the probed molecules have an absorption band matching the plasmon band of the tip.

The following question naturally arises: would investigations on distinct fluorophores, with different absorption bands, require the use of different tips, each with a plasmon band matching the absorption band of the fluorophore in question? We speculate that this can potentially be avoided by implementing clever strategies where the absorption/plasmon band of the tip can be tuned. Such a potential strategy can eventually rely on previous work showing that submicrometer particle-based structures can be employed to reconfigure photonic devices by external photonic radiation. One of the device configurations that was previously demonstrated involved metallic NPs or nanorods incorporated into a semiconducting structured matrix that exhibits strong plasmonic resonance, which depends on the power of the external photonic radiation that is being absorbed by the matrix.¹⁰⁴ Taking inspiration from this previous work, future specialized TEN probes can be designed to feature optical tunability obtained by adding an external control beam that, when absorbed in a silicon part of the tip nanostructure, will produce free electrons, leading to tuning of the plasmonic resonance of the nanostructure at the end of the tip, thus improving the energy transfer process by properly matching the plasmonic resonance to the plasmonic excitation wavelength. Given that such tips will possess a tunable plasmon band, the same tip will be capable of imaging various fluorescent molecules. In addition to its use for fluorescence imaging, this strategy could also enable subnanometer imaging of nonfluorescent materials.

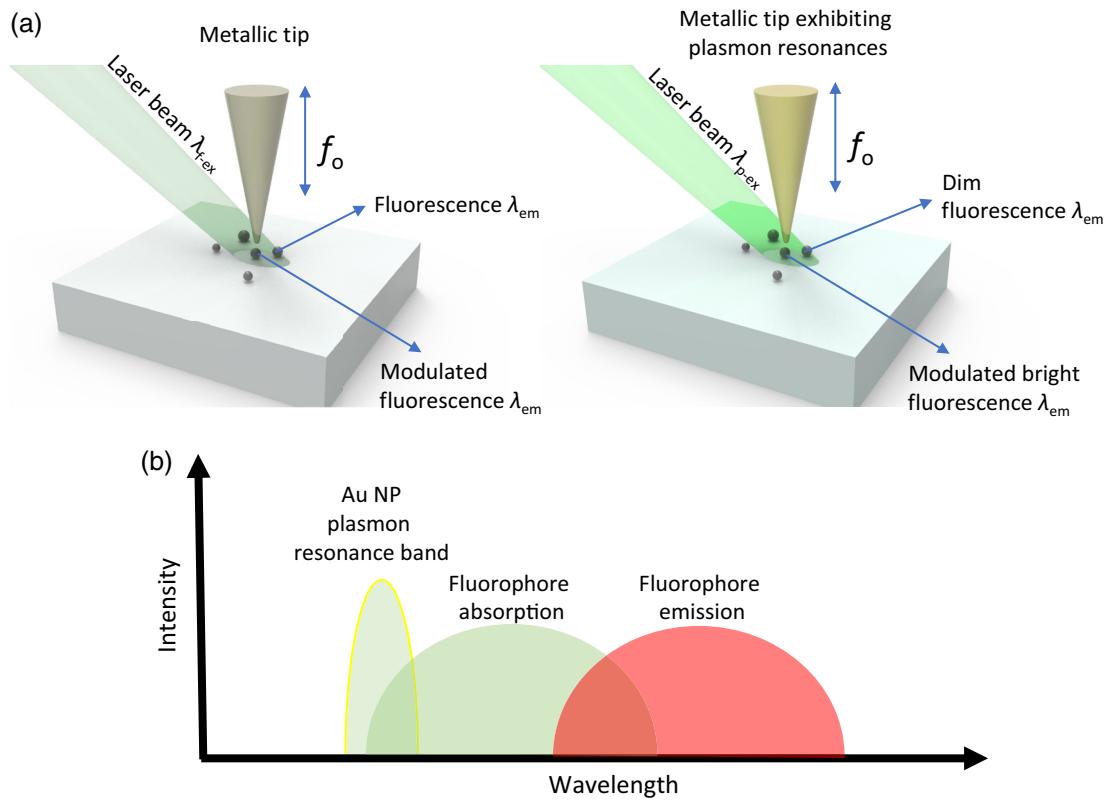


Fig. 10 (a) Conventional tip-enhanced fluorescence (left) versus tip-enhanced fluorescence based on PRET (right). In conventional TEF, the optical properties of the tip are not considered, and the excitation (λ_{f-ex}) is tuned to the maximum of the absorption band of the fluorescent molecule of interest. With PRET-based TEF, the laser beam used for excitation (λ_{p-ex}) matches the plasmon band of the tip, and fluorescence is obtained by dual effect, direct illumination, and PRET from tip (donor) to sample (acceptor), thus reducing the background and yielding higher SNR. (b) Condition for the PRET effect to take place. The plasmon resonance band overlaps with the fluorophore absorption band. When the plasmon band is positioned on the left tail of the absorption spectrum, the excitation light has a low contribution on the emission of illuminated fluorophores not benefiting from the PRET effect (those positioned far from the tip). Conversely, fluorophores under the tip would exhibit stronger emission due to the dual PRET and direct excitation effects.

On a different train of thought, we refer to probably the most well-known TEN technique, *s*-SNOM. The working principles of *s*-SNOM rely on a sharp tip that is scanned across the sample's surface while it is being excited with a focused laser beam. The attainable resolution in *s*-SNOM depends on the size and geometry of the probe, with many important applications having been reported for tip sizes ranging between 5 and 150 nm.^{82,91,105,106} The tip converts the incident radiation into a highly localized and enhanced near field at the tip apex, which modifies both the amplitude and the phase of the scattered light via the near-field interaction with the sample underneath.¹⁴ This process depends on the local dielectric properties of the tip and sample. The default way of extracting *s*-SNOM signals is by lock-in detection of the optical signals corresponding to the tip-sample interaction, which are modulated by the tapping movement of the tip.¹⁴ We speculate that this type of modulation, achieved by mechanical means, can be replaced, or augmented with an alternative/additional modulation scheme, by means of a pump beam tuned to the plasmon band of the tip, which can intermittently plasmonically activate/deactivate the tip, at ultrafast rates, and depending on the properties of the

sample, it can modify the interaction of the two mirror dipoles (in probe and sample) accounting for *s*-SNOM contrast.^{107,108} This pump beam would complement the probe beam, which in many *s*-SNOM applications is tuned to the absorption band of the sample to promote phase contrast.^{14,43,81,109} An additional layer of (faster) modulation can eventually provide higher SNR. Furthermore, this alternative modulation scheme based on on-off switching of the pump beam could even entirely replace the traditional modulation schemes based on the tapping movement of the probe, which could enable *s*-SNOM imaging in contact mode, which would be faster than tapping-mode *s*-SNOM (which is the current default way of performing *s*-SNOM investigations), and more suited for some applications, depending on the sample type and scanning environment. In addition to considering the tip's absorption as the key for signal modulation, referring to its scattering can also represent a route. For example, by intermittently using two close wavelengths, accounting for significantly different scattering-levels from the tip, we speculate that the *s*-SNOM signals can be modulated as well. Similar modulation approaches can eventually be implemented for other TEN modalities, such as TERS and PiFM. Overall,

we consider that having at hand probes with precisely known optical properties can open an entire new palette of data acquisition strategies for TEN techniques that can enable better outputs in terms of signal quality, sensitivity, robustness, and speed. Future work refining this technology from the plasmon coupling perspective¹¹⁰ will be important.

In addition to imaging, the interaction between focused light and AFM probes was also demonstrated in highly useful nanolithography and ablation purposes.^{97,98,111} We argue that in such applications, the use of optically resolved probes can also be important in optimizing the outputs, as the interactions between tip and sample are likely to be entirely different for situations when the illumination wavelength matches or not the absorption or scattering of the tip. Furthermore, these properties can potentially also be correlated with the heating profiles of the tip, which were previously shown to have an important impact over the final outputs of tip-enhanced nanoablation.¹¹²

Finally, we turn our attention to the issue of attainable resolution. Although the results presented here do not align, in terms of tip size, to the state-of-the-art on AFM probe sharpness, the motivation behind this proof-of-concept experiment was not aimed at addressing this particular problem. We speculate that adjusting our proposed methodology to incorporate the use of probes with different geometries, in combination with different processing methods, can eventually result in sharper probes. However, we find noteworthy to recall recent results,⁸² which show that tip sharpness is not always preferred. Thus we consider that having a precise understanding of the tip's optical properties can at times be the better option to consider.

5 Conclusions

Tip-enhanced nanoscopies have enabled so far a wide palette of discoveries and account for new scientific breakthroughs each day. However, they rely on nonspecialized probes, usually designed and commercialized for various nonoptical scanning probe microscopy variants, which significantly biases their potential. Here we propose the concept of TEN probes with known optical properties. To this end, we custom modified two commercial AFM probes to equip their apex with an NP, whose absorption and scattering properties we approximated by numerical simulations in COMSOL, based on Mie scattering.^{113,114} We argue that the so-developed probes, with resolved optical properties, can enable various data acquisition schemes for faster and more sensitive TEN imaging and may also prove useful for nanolithography. A series of perspectives in this regard are discussed. Overall, we consider the reported framework to be highly flexible, allowing the design and fabrication of a wide range of tips with custom-tailorable optical properties exhibiting various geometries and material compositions.

Disclosures

The authors declare that they have no known competing financial interests or personal relationships that could have appeared to influence the work reported in this paper.

Acknowledgments

SGS, DET and GAS acknowledge the support of the Romanian Executive Agency for Higher Education, Research, Development and Innovation Funding (Grant Nos. RO-NO-2019-0601 MEDYCONAI and PN-III-P1-1.1-TE-2019-1339 OPTIGAN),

and the support of Horizon 2020 Attract (Phase 1) via the TEF-PLASNOM project. SGS acknowledges as well support from the CA19118 EsSENce COST Action, and expresses sincere thanks to Dr. Xinzhong Chen (Stony Brook University) for help with Fig. 10 artwork.

References

1. Y. M. Sigal, R. Zhou, and X. Zhuang, "Visualizing and discovering cellular structures with super-resolution microscopy," *Science* **361**, 880–887 (2018).
2. M. B. Stone, S. A. Shelby, and S. L. Veatch, "Super-resolution microscopy: shedding light on the cellular plasma membrane," *Chem. Rev.* **117**, 7457–7477 (2017).
3. L. Schermelleh et al., "Super-resolution microscopy demystified," *Nat. Cell Biol.* **21**, 72 (2019).
4. Y. Jing et al., "Super-resolution microscopy: shedding new light on in vivo imaging," *Front. Chem.* **9**, 746900 (2021).
5. S. Pujals et al., "Super-resolution microscopy as a powerful tool to study complex synthetic materials," *Nat. Rev. Chem.* **3**, 68–84 (2019).
6. S. W. Hell et al., "The 2015 super-resolution microscopy roadmap," *J. Phys. D: Appl. Phys.* **48**, 443001 (2015).
7. K. C. Gwosch et al., "MINFLUX nanoscopy delivers 3D multi-color nanometer resolution in cells," *Nat. Meth.* **17**, 217–224 (2020).
8. M. Weber et al., "MINSTED nanoscopy enters the Ångström localization range," *Nat. Biotechnol.* (2022).
9. S. Castelletto and A. Boretti, "Color centers in wide-bandgap semiconductors for subdiffraction imaging: a review," *Adv. Photonics* **3**, 054001 (2021).
10. J. Vogelsang et al., "Make them blink: probes for super-resolution microscopy," *ChemPhysChem* **11**, 2475–2490 (2010).
11. S. Sreedharan et al., "Nanocarriers used as probes for super-resolution microscopy," *Mater. Chem. Front.* **5**, 1268–1282 (2021).
12. S. Wäldchen et al., "Light-induced cell damage in live-cell super-resolution microscopy," *Sci. Rep.* **5**, 14348 (2015).
13. M. Cosentino et al., "AFM-STED correlative nanoscopy reveals a dark side in fluorescence microscopy imaging," *Sci. Adv.* **5**, eaav8062 (2019).
14. X. Chen et al., "Modern scattering-type scanning near-field optical microscopy for advanced material research," *Adv. Mater.* **31**, 1804774 (2019).
15. P. Verma, "Tip-enhanced Raman spectroscopy: technique and recent advances," *Chem. Rev.* **117**, 6447–6466 (2017).
16. J. M. Gerton et al., "Tip-enhanced fluorescence microscopy at 10 nanometer resolution," *Phys. Rev. Lett.* **93**, 180801 (2004).
17. A. Zayats and V. Sandoghdar, "Apertureless near-field optical microscopy via local second-harmonic generation," *J. Microsc.* **202**, 94–99 (2001).
18. K. Yao et al., "Nanoscale optical imaging of 2D semiconductor heterostructures by exciton enhanced second harmonic generation," *Bull. Am. Phys. Soc.* **67**(3) (2022).
19. B. Yang et al., "Sub-nanometre resolution in single-molecule photoluminescence imaging," *Nat. Photonics* **14**, 693–699 (2020).
20. D. Nowak et al., "Nanoscale chemical imaging by photoinduced force microscopy," *Sci. Adv.* **2**, e1501571 (2016).
21. D. A. Schmidt, I. Kopf, and E. Bruendermann, "A matter of scale: from far-field microscopy to near-field nanoscopy," *Laser Photonics Rev.* **6**, 296–332 (2012).
22. S. Mahapatra et al., "Tip-enhanced Raman spectroscopy: chemical analysis with nanoscale to angstrom scale resolution," *J. Chem. Phys.* **153**, 010902 (2020).
23. P. Kusch et al., "Combined tip-enhanced Raman spectroscopy and scattering-type scanning near-field optical microscopy," *J. Phys. Chem. C* **122**, 16274–16280 (2018).

24. X. G. Xu and M. B. Raschke, "Near-field infrared vibrational dynamics and tip-enhanced decoherence," *Nano Lett.* **13**, 1588–1595 (2013).
25. E. A. Muller, B. Pollard, and M. B. Raschke, "Infrared chemical nano-imaging: accessing structure, coupling, and dynamics on molecular length scales," *J. Phys. Chem. Lett.* **6**, 1275–1284 (2015).
26. H. Lee et al., "Tip-enhanced photoluminescence nano-spectroscopy and nano-imaging," *Nanophotonics* **9**, 3089–3110 (2020).
27. M. Ohtsu, "History, current developments, and future directions of near-field optical science," *Opto-Electron. Adv.* **3**, 190046 (2020).
28. A. P. Hibbins, J. R. Sambles, and C. R. Lawrence, "Surface plasmon-polariton study of the optical dielectric function of titanium nitride," *J. Mod. Opt.* **45**, 2051–2062 (1998).
29. B. Knoll and F. Keilmann, "Enhanced dielectric contrast in scattering-type scanning near-field optical microscopy," *Opt. Commun.* **182**, 321–328 (2000).
30. A. A. Govyadinov et al., "Quantitative measurement of local infrared absorption and dielectric function with tip-enhanced near-field microscopy," *J. Phys. Chem. Lett.* **4**, 1526–1531 (2013).
31. D. E. Tranca et al., "High-resolution quantitative determination of dielectric function by using scattering scanning near-field optical microscopy," *Sci. Rep.* **5**, 11876 (2015).
32. M. M. Qazilbash et al., "Mott transition in VO₂ revealed by infrared spectroscopy and nano-imaging," *Science* **318**, 1750–1753 (2007).
33. Z. Fei et al., "Gate-tuning of graphene plasmons revealed by infrared nano-imaging," *Nature* **487**, 82–85 (2012).
34. I. Amenabar et al., "Structural analysis and mapping of individual protein complexes by infrared nanospectroscopy," *Nat. Commun.* **4**, 2890 (2013).
35. M. Liu et al., "Anisotropic electronic state via spontaneous phase separation in strained vanadium dioxide films," *Phys. Rev. Lett.* **111**, 096602 (2013).
36. C. Westermeyer et al., "Sub-micron phase coexistence in small-molecule organic thin films revealed by infrared nano-imaging," *Nat. Commun.* **5**, 4101 (2014).
37. E. Yoxall et al., "Direct observation of ultraslow hyperbolic polariton propagation with negative phase velocity," *Nat. Photonics* **9**, 674 (2015).
38. J. N. Chen et al., "Optical nano-imaging of gate-tunable graphene plasmons," *Nature* **487**, 77–81 (2012).
39. Z. Fei et al., "Gate-tuning of graphene plasmons revealed by infrared nano-imaging," *Nature* **487**, 82–85 (2012).
40. T. Neuman et al., "Mapping the near fields of plasmonic nano-antennas by scattering-type scanning near-field optical microscopy," *Laser Photonics Rev.* **9**, 637–649 (2015).
41. R. O. Freitas et al., "Nano-infrared imaging of primary neurons," *Cells* **10**, 2559 (2021).
42. K. J. Kaltenecker et al., "Infrared-spectroscopic, dynamic near-field microscopy of living cells and nanoparticles in water," *Sci. Rep.* **11**, 21860 (2021).
43. K. Kanevche et al., "Infrared nanoscopy and tomography of intracellular structures," *Commun. Biol.* **4**, 1–8 (2021).
44. E. Pfitzner and J. Heberle, "Infrared scattering-type scanning near-field optical microscopy of biomembranes in water," *J. Phys. Chem. Lett.* **11**, 8183–8188 (2020).
45. D. E. Tranca et al., "Nanoscale mapping of refractive index by using scattering-type scanning near-field optical microscopy," *Nanomed.: Nanotechnol. Biol. Med.* **14**, 47–50 (2018).
46. W. Zhang and Y. Chen, "Visibility of subsurface nanostructures in scattering-type scanning near-field optical microscopy imaging," *Opt. Express* **28**, 6696–6707 (2020).
47. K. Moon et al., "Subsurface nanoimaging by broadband terahertz pulse near-field microscopy," *Nano Lett.* **15**, 549–552 (2015).
48. H. Wang et al., "Mapping three-dimensional near-field responses with reconstruction scattering-type scanning near-field optical microscopy," *AIP Adv.* **7**, 055118 (2017).
49. P. Bazylewski, S. Ezugwu, and G. Fanchini, "A review of three-dimensional scanning near-field optical microscopy (3D-SNOM) and its applications in nanoscale light management," *Appl. Sci.* **7**, 973 (2017).
50. M. S. Anderson, "Locally enhanced Raman spectroscopy with an atomic force microscope," *Appl. Phys. Lett.* **76**, 3130–3132 (2000).
51. N. Hayazawa et al., "Metallized tip amplification of near-field Raman scattering," *Opt. Commun.* **183**, 333–336 (2000).
52. R. M. Stöckle et al., "Nanoscale chemical analysis by tip-enhanced Raman spectroscopy," *Chem. Phys. Lett.* **318**, 131–136 (2000).
53. G. G. Hoffmann et al., "Tip-enhanced Raman mapping of single-walled carbon nanotube networks in conductive composite materials," *J. Raman Spectrosc.* **48**, 191–196 (2017).
54. Y. Okuno et al., "Tip-enhanced Raman investigation of extremely localized semiconductor-to-metal transition of a carbon nanotube," *Phys. Rev. Lett.* **111**, 216101 (2013).
55. T. A. Yano et al., "Tip-enhanced nano-Raman analytical imaging of locally induced strain distribution in carbon nanotubes," *Nat. Commun.* **4**, 2592 (2013).
56. J. Rogalski et al., "STM tip-enhanced Raman spectroscopy and the investigation of doped grapheme," *Vibr. Spectrosc.* **91**, 128–135 (2017).
57. T. A. Yano et al., "Pressure-assisted tip-enhanced Raman imaging at a resolution of a few nanometers," *Nat. Photonics* **3**, 473–477 (2009).
58. C. Chen, N. Hayazawa, and S. Kawata, "A 1.7 nm resolution chemical analysis of carbon nanotubes by tip-enhanced Raman imaging in the ambient," *Nat. Commun.* **5**, 3312 (2014).
59. A. Ambrosio et al., "Observation of nanoscale refractive index contrast via photoinduced force microscopy," *ACS Photonics* **4**, 846–851 (2017).
60. T. Schmid et al., "Towards chemical analysis of nanostructures in biofilms II: tip-enhanced Raman spectroscopy of alginates," *Anal. Bioanal. Chem.* **391**, 1907–1916 (2008).
61. D. Cialla et al., "Raman to the limit: tip-enhanced Raman spectroscopic investigations of a single tobacco mosaic virus," *J. Raman Spectrosc.* **40**, 240–243 (2009).
62. A. Hermelink et al., "Towards a correlative approach for characterising single virus particles by transmission electron microscopy and nanoscale Raman spectroscopy," *Analyst* **142**, 1342–1349 (2017).
63. U. Neugebauer et al., "On the way to nanometer-sized information of the bacterial surface by tip-enhanced Raman spectroscopy," *ChemPhysChem* **7**, 1428–1430 (2006).
64. B. R. Wood et al., "Tip-enhanced Raman scattering (TERS) from hemozoin crystals within a sectioned erythrocyte," *Nano Lett.* **11**, 1868–1873 (2011).
65. L. F. Xiao et al., "Probing membrane receptor-ligand specificity with surface- and tip-enhanced Raman scattering," *Anal. Chem.* **89**, 9091–9099 (2017).
66. R. Böhme et al., "Biochemical imaging below the diffraction limit-probing cellular membrane related structures by tip-enhanced Raman spectroscopy (TERS)," *J. Biophotonics* **3**, 455–461 (2010).
67. A. V. Zayats and V. Sandoghdar, "Apertureless scanning near-field second-harmonic microscopy," *Opt. Commun.* **178**, 245–249 (2000).
68. C. C. Neacsu et al., "Second-harmonic near-field imaging of ferroelectric domain structure of YMnO₃," *Phys. Rev. B* **79**, 100107 (2009).
69. J. Jahng et al., "Linear and nonlinear optical spectroscopy at the nanoscale with photoinduced force microscopy," *Acc. Chem. Res.* **48**, 2671–2679 (2015).
70. T. U. Tumkur et al., "Photoinduced force mapping of plasmonic nanostructures," *Nano Lett.* **16**, 7942–7949 (2016).
71. M. Soliman et al., "Photoinduced force microscopy: a technique for hyperspectral nanochemical mapping," *Jpn. J. Appl. Phys.* **56**, 08LA04 (2017).

72. J. Jahng et al., “Visualizing surface plasmon polaritons by their gradient force,” *Opt. Lett.* **40**, 5058–5061 (2015).
73. L. Zhang et al., “Transformable peptide nanoparticles arrest HER2 signalling and cause cancer cell death in vivo,” *Nat. Nanotechnol.* **15**, 145–153 (2020).
74. Z. Ma et al., “Fluorescence near-field microscopy of DNA at sub-10 nm resolution,” *Phys. Rev. Lett.* **97**, 260801 (2006).
75. O. Schulz et al., “Tip induced fluorescence quenching for nanometer optical and topographical resolution,” *Opt. Nanosc.* **2**, 1–8 (2013).
76. A. Harder et al., “Apertureless scanning near-field optical microscopy of sparsely labeled tobacco mosaic viruses and the intermediate filament desmin,” *Beilstein J. Nanotechnol.* **4**, 510–516 (2013).
77. C. Xie et al., “Tip-enhanced fluorescence microscopy of high-density samples,” *Appl. Phys. Lett.* **89**, 143117 (2006).
78. F. M. Huang, F. Festy, and D. Richards, “Tip-enhanced fluorescence imaging of quantum dots,” *Appl. Phys. Lett.* **87**, 183101 (2005).
79. E. J. Sánchez, L. Novotny, and X. S. Xie, “Near-field fluorescence microscopy based on two-photon excitation with metal tips,” *Phys. Rev. Lett.* **82**, 4014 (1999).
80. L. Meng et al., “A nanoplasmonic strategy for precision in-situ measurements of tip-enhanced Raman and fluorescence spectroscopy,” *Sci. Rep.* **6**, 19558 (2016).
81. S. G. Stanciu et al., “Scattering-type scanning near-field optical microscopy of polymer-coated gold nanoparticles,” *ACS Omega* **7**, 11353–11362 (2022).
82. C. Maisson et al., “Probes for ultrasensitive THz nanoscopy,” *ACS Photonics* **6**, 1279–1288 (2019).
83. COMSOL Multiphysics, *Introduction to COMSOL Multiphysics*®, p. 32, COMSOL Multiphysics, Burlington, Massachusetts (1998).
84. T. Siday et al., “Resonance-enhanced terahertz nanoscopy probes,” *ACS Photonics* **7**, 596–601 (2020).
85. I. U. Vakarelski and K. Higashitani, “Single-nanoparticle-terminated tips for scanning probe microscopy,” *Langmuir* **22**, 2931–2934 (2006).
86. C. Leiterer et al., “High precision attachment of silver nanoparticles on AFM tips by dielectrophoresis,” *Anal. Bioanal. Chem.* **408**, 3625–3631 (2016).
87. O. K. Ong and I. Sokolov, “Attachment of nanoparticles to the AFM tips for direct measurements of interaction between a single nanoparticle and surfaces,” *J. Colloid Interface Sci.* **310**, 385–390 (2007).
88. R. M. Langford et al., “Focused ion beam micro- and nanoengineering,” *MRS Bull.* **32**, 417–423 (2007).
89. J. Melngailis, “Focused ion beam technology and applications,” *J. Vac. Sci. Technol. B: Microelectron. Process. Phenom.* **5**, 469–495 (1987).
90. X. Chen et al., “Rapid simulations of hyperspectral near-field images of three-dimensional heterogeneous surfaces—part II,” *Opt. Express* **30**, 11228–11242 (2022).
91. S. Mastel et al., “Understanding the image contrast of material boundaries in IR nanoscopy reaching 5 nm spatial resolution,” *ACS Photonics* **5**, 3372–3378 (2018).
92. P. Hildebrandt et al., “Alternative fluorescent labeling strategies for characterizing gram-positive pathogenic bacteria: flow cytometry supported counting, sorting, and proteome analysis of *Staphylococcus aureus* retrieved from infected host cells,” *Cytometry A* **89**, 932–940 (2016).
93. W. Telford et al., “DPSS yellow-green 561-nm lasers for improved fluorochrome detection by flow cytometry,” *Cytometry A* **68**, 36–44 (2005).
94. S. A. Maier, *Plasmonics: Fundamentals and Applications*, Springer, New York (2007).
95. G. L. Liu et al., “Quantized plasmon quenching dips nanospectroscopy via plasmon resonance energy transfer,” *Nat. Methods* **4**, 1015–1017 (2007).
96. B. Deutsch, R. Hillenbrand, and L. Novotny, “Near-field amplitude and phase recovery using phase-shifting interferometry,” *Opt. Express* **16**, 494–501 (2008).
97. W. Lee et al., “A rewritable optical storage medium of silk proteins using near-field nano-optics,” *Nat. Nanotechnol.* **15**, 941–947 (2020).
98. F. Cao, F. Donnarumma, and K. K. Murray, “Wavelength-dependent atomic force microscope tip-enhanced laser ablation,” *Appl. Surf. Sci.* **447**, 437–441 (2018).
99. T. Lewi et al., “Widely tunable infrared antennas using free carrier refraction,” *Nano Lett.* **15**, 8188–8193 (2015).
100. J. Mock et al., “Shape effects in plasmon resonance of individual colloidal silver nanoparticles,” *J. Chem. Phys.* **116**, 6755–6759 (2002).
101. J. Dong et al., “Recent progress on plasmon-enhanced fluorescence,” *Nanophotonics* **4**, 472–490 (2015).
102. P. Pompa et al., “Metal-enhanced fluorescence of colloidal nanocrystals with nanoscale control,” *Nat. Nanotechnol.* **2**, 126–130 (2006).
103. S. G. Stanciu et al., “A novel approach for near-field optical microscopy based on tip-enhanced fluorescence via plasmon resonance energy transfer (TEFPLASNO),” in *Proc. ATTRACT - Final Conf. Igniting Deep Tech Revol.*, pp. 1–6 (2020).
104. A. Shahmoon, A. Meiri, and Z. Zalevsky, “Sub-micron particle based structures as reconfigurable photonic devices controllable by external photonic and magnetic fields,” *Sensors* **11**, 2740–2750 (2011).
105. R. Büchner et al., “Tip coupling and array effects of gold nanoantennas in near-field microscopy,” *ACS Photonics* **8**, 3486–3494 (2021).
106. S. G. Stanciu et al., “Characterization of nanomaterials by locally determining their complex permittivity with scattering-type scanning near-field optical microscopy,” *ACS Appl. Nano Mater.* **3**, 1250–1262 (2020).
107. F. Keilmann and R. Hillenbrand, “Near-field microscopy by elastic light scattering from a tip,” *Philos. Trans. R. Soc. Lond. Ser. A: Math. Phys. Eng. Sci.* **362**, 787–805 (2004).
108. X. Guo, K. Bertling, and A. D. Rakić, “Optical constants from scattering-type scanning near-field optical microscope,” *Appl. Phys. Lett.* **118**, 041103 (2021).
109. K. G. Wirth et al., “Tunable s-SNOM for nanoscale infrared optical measurement of electronic properties of bilayer graphene,” *ACS Photonics* **8**, 418–423 (2021).
110. Q. Sun et al., “Revealing the plasmon coupling in gold nanochains directly from the near field,” *Opto-Electron. Adv.* **2**, 18003001 (2019).
111. S. Ghorai, C. A. Seneviratne, and K. K. Murray, “Tip-enhanced laser ablation sample transfer for biomolecule mass spectrometry,” *J. Am. Soc. Mass Spectrom.* **26**, 63–70 (2014).
112. K. Zhang, “A method for reducing laser heating on atomic force microscope tips,” *Eur. Phys. J.-Appl. Phys.* **53**, 10603 (2011).
113. M. Fowler, “AltaSim simulates Mie scattering of electromagnetic waves,” Comsol Application Libraries, COMSOL Blog, <https://www.comsol.com/blogs/altasim-simulates-mie-scattering-electromagnetic-waves/> (accessed 22 July 2014).
114. J. Crompton, S. Yushanov, and K. Koppenhoefer, “Mie scattering of electromagnetic waves,” Comsol Technical Papers and Publications, 2013, <https://www.comsol.com/paper/mie-scattering-of-electromagnetic-waves-15917>.

Jeremy Belhassen received his BSc degree in physics in 2016 and his MSc degree in fundamental physics in 2019 from the Université Grenoble-Alpes, France, with a specialization in photonics/semiconductors with Phelma partnership. His MSc thesis was an international exchange with Jerusalem College of Technology (JCT). He is a PhD candidate at Bar-Ilan-University and JCT, under the joint supervision of Prof. Zeev Zalevsky and Dr. Avi Karsenty, and a research assistant at

the Advanced Laboratory of Electro-Optics (ALEO) of JCT, working on nanophotonics/nanoelectronics devices development.

Simi Glass is a BSc student in electrical engineering at JCT, with a specialization in power supplies. He won the first place in the 2022 Israel Electric Corporation Student Contest, as part of the JCT team. He is a research assistant at the ALEO of JCT, under the supervision of Dr. Avi Karsenty, and is currently working on various projects involving micro/nanoscale material conductivity.

Eti Teblum received her PhD from Bar-Ilan University, Israel, in 2009. Her research experience includes polymers, organic chemistry synthesis, and materials science. She specialized in synthesizing 1D materials as CNT and CNF, and 2D materials as graphene and TMDs, by CVD and wet chemistry. In 2017, she joined BINA as an AFM expert. Currently, she is BINA's project manager and continues to operate the AFM unit at BINA. She has authored 34 scientific papers.

George A. Stanciu is a professor of physics at the University Politehnica of Bucharest. He received the Professor title in 1994. Since 1973, he has been working in the laser scanning microscopy field. His team reported the first digital laser scanning microscope. He is the head of the Center for Microscopy-Microanalysis and Information Processing. Lately, he is focused on different scanning laser microscopy techniques: instrumentation and applications. He is a senior member of the IEEE from 1995.

Denis-Emanuil Tranca has graduated the Faculty of Electronics, Telecommunications and Information Technology at the University Politehnica of Bucharest in 2010 and received his master's degree in diploma in the field of optoelectronics from the same university two years later. In 2015, he defended his PhD thesis that was dealing with new detection and investigation applications for scattering scanning near-field

optical microscopy. He has been involved in the research activities that take place at CMMIP-UPB since November 2011.

Zeev Zalevsky received his BSc and direct PhD degrees in electrical engineering from Tel-Aviv University in 1993 and 1996, respectively. He is currently a full professor and the dean of engineering at Bar-Ilan University, Israel. His major fields of research are optical super-resolution, biomedical optics, and nanophotonics. For his research, he received many national/international prizes and he is a fellow of many large scientific societies, SPIE, Optica, IEEE, EOS, NAI, and more.

Stefan G. Stanciu received his PhD in electronic engineering and is habilitated in physics. He currently acts as a senior researcher at the Center for Microscopy-Microanalysis and Information Processing of Politehnica University of Bucharest, being involved in research focusing, among others, on optical nanoscopy, biophotonics, advanced materials, and on AI-methods for high-resolution imaging. He has authored >70 WOS journal articles and currently serves as a senior editor for *IEEE Photonics Journal* and an associate editor for *Frontiers in Photonics*.

Avi Karsenty received his PhD in applied-physics/material-science (microelectronics/electro-optics divisions) from Hebrew University of Jerusalem Israel (HUJI) in 2003. He has more than two decades of experience in high-tech-industry in Europe and Israel, having spent years with Intel (1995 to 2011) in senior engineering/management. Back to academia (2011), he served as the head of the Applied-Physics/Electro-Optics Department (2014 to 2018) at JCT. He is an IEEE/Optica senior member, holding 40 awards in engineering/physics with >70 journal publications. He shares expertise in nanophotonics/nanoelectronics devices, quality and reliability, and super-resolution techniques. He leads the JCT Nanotechnology Center.